



1 **Detecting seasonal and long-term vertical displacement in the North**

2 **China Plain using GRACE and GPS**

3

4 Linsong Wang<sup>1,2</sup>, Chao Chen<sup>1,2</sup>, Jinsong Du<sup>1</sup>, and Tongqing Wang<sup>3</sup>

5 <sup>1</sup>Hubei Subsurface Multi-scale Imaging Lab (SMIL), Institute of Geophysics and Geomatics, China

6 University of Geosciences, Wuhan, Hubei, China

7 <sup>2</sup>Three Gorges Research Center for Geo-hazard, Ministry of Education, China University of

8 Geosciences, Wuhan, Hubei, China

9 <sup>3</sup>First Crust Deformation Monitoring and Administration Center, China Earthquake Administration,

10 Tianjin, China

11

12 \* Corresponding author: Linsong Wang, [wanglinsong@cug.edu.cn](mailto:wanglinsong@cug.edu.cn)

13

14 **Abstract:**

15 We employ twenty-nine continuous Global Positioning System (GPS) time series data

16 together with data from Gravity Recovery and Climate Experiment (GRACE) are analyzed to

17 determine the seasonal displacements of surface loadings in the NCP. Results show significant

18 seasonal variations and a strong correlation between GPS and GRACE results in the vertical

19 displacement component; the average correlation and WRMS reduction between GPS and

20 GRACE are 75.6% and 28.9%, respectively, when atmospheric and non-tidal ocean effects

21 were removed, but the peak to peak annual amplitude of GPS (1.2~6.3 mm) is greater than

22 GRACE-derived (1.0~2.2 mm). We also calculate the trend rate as well as the seasonal signal



23 caused by the mass load change from GRACE data, the rate of GRACE-derived Terrestrial  
24 Water Storage (TWS) loss (after multiplying by the scaling factor) in the NCP was 3.39 cm/yr  
25 (equivalent to 12.42 km<sup>3</sup>/yr) from 2003 to 2009. For a 10-year time span (2003 to 2012), the  
26 rate was 2.57 cm/yr (equivalent to 9.41 km<sup>3</sup>/yr). Basing on spherical harmonic coefficients for  
27 the gravity field and load Love numbers, we use GRACE model to remove the vertical rates  
28 of elastic displacements due to the surface mass change from GPS data. An overall uplift for  
29 the whole region at the 0.04–1.47 mm/yr level from 2004 to 2009, but the rate of change  
30 direction is inconsistent in different GPS stations at -0.94–2.55 mm/yr level from 2010 to  
31 2013.

32

33 **Keywords:** GPS, GRACE, Seasonal and long-term displacement, Terrestrial water storage,  
34 the North China Plain

35

## 36 **1. Introduction**

37 Using Global Positioning System (GPS) to monitor crustal motion, especially in the vertical  
38 or height component due to its large amplitude, has been used to study surface loading caused  
39 by mass change. Site-position time series recorded by continuous GPS arrays have revealed  
40 that vertical displacement variations can result from trend or seasonal distribution of mass in a  
41 region or global changes that cause displacement of the Earth's surface (e.g., a change of  
42 continental water [Bevis et al., 2005; van Dam et al., 2007; Wahr et al., 2013], ice [Sauber et  
43 al., 2000; Khan et al., 2010; Nielsen et al., 2013], snow [Heki, 2001; Grapenthin et al., 2006],  
44 ocean [van Dam et al., 2012; Wahr et al., 2014] and atmospheric mass [van Dam et al., 1994;



45 Boehm et al., 2007]).

46

47 On the global scale, terrestrial hydrologic mass exchanges, that causes significant large-scale  
48 loading, occur between the oceans, continents, and atmosphere at seasonal and inter-annual  
49 time scales. On the local scale, inter-annual and long-periodic change in the hydrologic cycle  
50 that most significantly affects loading are large anthropogenic disturbances on groundwater  
51 extraction and artificial reservoir water impoundment and other climate-driven factors (e.g.,  
52 natural floods and droughts) [e.g., Chao et al., 2008; Rodell et al., 2009; Feng et al., 2013;  
53 Joodaki et al., 2014; Wang et al., 2014]. The global-scale mass variations closely related to  
54 changes in terrestrial water storage (TWS) are observed by the Gravity Recovery and Climate  
55 Experiment (GRACE) satellite mission, while the surface elastic displacement can be  
56 estimated if the load and rheological properties of the Earth were known [Farrell, 1972]. The  
57 majority of previous loading studies solved the three components of crustal motion by joint  
58 analysis of GRACE time-variable gravity field coefficients and GPS data [Kusche and  
59 Schrama, 2005; van Dam et al., 2007; Fu and Freymueller, 2012; Fu et al., 2013]. In principle  
60 the loading effects caused by the majority of mass redistributions near the Earth's surface are  
61 from water, atmospheric, and ocean transports on daily to inter-annual timescales [Kusche and  
62 Schrama, 2005]. The variations of the atmospheric and ocean contribution to the surface  
63 displacement can be reasonably modeled, and therefore corrected, using global atmospheric  
64 surface pressure data and space geodetic data, respectively. Thus, after removing the loading  
65 effects of the atmospheric and ocean, GRACE-derived displacement and GPS data allow the  
66 detection of changes in the Earth's larger hydrological storage systems.



67

68 In general, changes in TWS capacities depend on precipitation and human consumption.

69 Variations in TWS may be related to precipitation, which is strongly driven by climate and

70 can be simulated from global water and energy balance models [Syed et al., 2008]. This is

71 related to soil texture and root depth in the case of soil water storage (e.g., soil moisture and

72 vegetation canopy storage can be derived from the Global Land Data Assimilation System

73 (GLDAS) [Rodell et al., 2004], the WaterGAP Global Hydrology Model (WGHM) [Döll et al.,

74 2003] and the Community Land Model (CLM) [Oleson et al., 2013]), surface water storage

75 (e.g., water in rivers, lakes, reservoirs and wetlands can be derived from WGHM while snow

76 or ice can be derived from WGHM and CLM), and naturally occurring (i.e., climate-driven)

77 aquifer storage (e.g., groundwater predicted by WGHM and CLM). Variations in TWS may

78 also be caused by man-made factors, such as water withdrawals for irrigation purposes [Döll,

79 2009] and dam construction for power generation and navigation [Wang et al., 2011]. These

80 changes in TWS can be observed in situ (i.e., groundwater level and impounded water level).

81 All can cause variations in TWS can lead to the overall changes in crust displacement.

82

83 This study focuses on the crustal deformation of the North China Plain (NCP) (Figure 1),

84 which is one of the most uniformly and extensively altered areas by human activities in the

85 world [Tang et al., 2013]. The NCP is one of the world's largest aquifer systems and supports

86 an enormous exploitation of groundwater. Overexploitation of groundwater has seriously

87 affected agriculture irrigation, industry, public supply, and ecosystems in the NCP. Previous

88 studies used GRACE data, land surface models, and well observations to provide insight on



89 groundwater depletion in the NCP [Feng et al., 2013; Moiwo et al., 2013; Tang et al., 2013;  
90 Huang et al., 2015]. Liu et al. [2014] has discussed loading displacement in the NCP before.  
91 Only five GPS stations (i.e., BJFS, BJSH, JIXN, TAIN, and ZHNZ) data are used in their  
92 work. Although they calculated the seasonal amplitudes, phases and trends of vertical  
93 displacement from GRACE and GPS, the atmospheric and non-tidal ocean loading effects  
94 were not removed in the Liu et al.'s work, i.e., added the Atmosphere and Ocean De-aliasing  
95 Level-1B (AOD1B) solution (GAC solution) back to the GRACE spherical harmonic  
96 solutions.

97

98 Here, we use GRACE and data from 29 GPS sites to study the seasonal and long-term loading  
99 displacement due to dynamic hydrological processes and groundwater-derived land  
100 subsidence in the NCP. In contrast to previous focus study [Liu et al., 2014], the most obvious  
101 difference between our results and their work is we removed other loading effects (e.g.,  
102 atmospheric and non-tidal ocean) in order to reflect the seasonal and long-term displacement  
103 caused by TWS loads better. Additionally, we discuss long-term trend due to mass change  
104 revealed by GRACE measurements and its impacts on tectonic vertical rates evaluations.

105

## 106 **2. Data Analysis**

### 107 **2.1 GRACE Data**

108 The GRACE mission design makes it particularly useful for time-variable gravity studies.  
109 GRACE was jointly launched by NASA and the German Aerospace Center (DLR) in March  
110 2002 [Tapley et al., 2004a]. The Level-2 gravity products consist of complete sets of spherical



111 harmonic (Stokes) coefficients out to some maximum degree and order (typically  $l_{max} = 120$ )  
112 averaged over monthly intervals. When considering large-scale mass redistribution in the  
113 Earth system on a timescale ranging from weekly to interdecadal, it is reasonable to assume  
114 that all relevant processes occur in a thin layer at the Earth's surface [Kusche and Schrama,  
115 2005]. In this analysis, we assume that the gravitational and geometrical response of the Earth  
116 can be described by Farrell's [1972] theory, where the loads Love numbers only depend on  
117 the spherical harmonic degree. Thus, the elastic displacements due to the surface mass change  
118 can easily be represented in terms of spherical harmonic coefficients for the gravity field and  
119 load Love numbers,  $k_l$ ,  $l_l$ , and  $h_l$  [Wahr et al., 1998; Kusche and Schrama, 2005]. Level-2  
120 products are generated at several project-related processing centers, such as the Center for  
121 Space Research (CSR) at the University of Texas, GeoForschungsZentrum (CSR) in Potsdam,  
122 Germany, and the Jet Propulsion Laboratory (JPL) in California. The mass estimates (TWS  
123 and sea level) show very good agreement among these products [Fu and Freymueller, 2012;  
124 Wahr et al., 2014; Wang et al., 2014].  
125  
126 This study used monthly sets of spherical harmonic (Stokes) coefficients from GRACE RL05  
127 (i.e., Release 5) gravity field solutions generated from the CSR, spanning from February 2003  
128 to April 2013. Each monthly GRACE field consisted of a set of Stokes coefficients,  $C_{lm}$  and  
129  $S_{lm}$ , up to a degree and order ( $l$  and  $m$ ) of 60. In fact, the GRACE Stokes coefficients ("GSM"  
130 coefficients denoted by the GRACE Project) have had modeled estimates of the atmospheric  
131 and oceanic mass signals removed. Thus the GRACE coefficients include the full terrestrial  
132 water storage signal with remaining atmospheric and oceanic signals due to errors in the



133      respective models [Swenson et al., 2008]. Generally, using the GRACE AOD1B products can  
134      add back the de-aliasing atmospheric and non-tidal oceanic effects to the GRACE data.  
135      However, we would like to reduce the environmental loading contributions to the GRACE  
136      and GPS observations, if we study on the accurate interpretation of displacement due to TWS  
137      loading. Thus, we analyzed on the effects of non-tidal ocean variations and atmospheric  
138      loading on the GRACE model and GPS coordinates, please see Section S1 in the supporting  
139      information for details.

140

141      We replaced the GRACE  $C_{20}$  coefficients with  $C_{20}$  coefficients inferred from satellite laser  
142      ranging [Cheng et al., 2013]. Due to the fact that the reference frame origin used in the  
143      GRACE gravity field determination is the Earth's center of mass (CM), GRACE cannot  
144      determine the degree-1 terms variations in the Earth's gravity field (geocenter motion). Here,  
145      we used degree-1 coefficients as calculated by Swenson et al. [2008] to determine the position  
146      of the CM relative to the center of figure (CF) of the Earth's outer surface. We applied the  
147      post-processing method described in Swenson and Wahr [2006] to remove north-south stripes.  
148      We adopted 250 km as the averaging radius to implement Gaussian smoothing, a technique  
149      which suppresses errors at high degrees [Wahr et al., 1998; van Dam et al., 2007]. Stokes  
150      coefficients results from A et al. [2013] were used to remove contributions from Glacial  
151      Isostatic Adjustment (GIA). The contribution of GIA is about 0.28–0.33 mm/yr and  
152      non-seasonal in the NCP, which is small and non-seasonal; so their impact on the seasonal  
153      results discussed in this paper would be minimal, even if they were not removed.  
154      The spatial pattern of TWS, shown in Figure 2, was obtained from monthly GRACE mass



155 solutions for NCP and surrounding regions between spring, 2003, and spring, 2013. An  
156 obvious negative trend was identified localized over North China, including some of the  
157 Northwest regions (i.e., Shanxi province) and Northeast regions (i.e., Liaoning province). The  
158 TWS changes derived from the GRACE data show significant loss trends across the entire  
159 study area (NCP), specifically in Beijing, Tianjin, Hebei province, and Shanxi province.  
160 Previous studies have investigated how much groundwater depletion has caused the  
161 GRACE-derived TWS loss in the whole of the NCP [Feng et al., 2013; Moiwo et al., 2013] or  
162 in different sub-regions of the NCP [Tang et al., 2013; Huang et al., 2015]. These  
163 investigations, however, did not focus on regional displacement due to seasonal or long term  
164 variations of hydrologic loading.

165

## 166 **2.2 GPS Data**

167 Twenty-four GPS sites from the Crustal Movement Observation Network of China  
168 (CMONOC) and five GPS sites from the International GNSS Service (IGS) (Table 1) were  
169 analyzed in this study (Figure 1 shows the locations of the GPS stations). Eight GPS sites of  
170 them were located in the surrounding area of the NCP. Daily values for the upward, eastward  
171 and northward coordinates were determined by GPS data of IGS stations between 2003 and  
172 2013, which is consistent with GRACE time span. The 24 GPS sites of CMONOC provided  
173 data from 2010 to 2013. GIPSY/OASIS-II (Version 5.0) software was used in point  
174 positioning mode to obtain the daily coordinates and covariances; these were used to  
175 transform the daily values into ITRF2008 [Altamimi et al., 2011]. We estimated this daily  
176 frame alignment transformation using a set of reliable ITRF stations (~10 stations each day).



177 In the GPS processing, corrections for solid Earth tides were undertaken, and ocean tide  
178 loading effects were corrected using ocean tide model FES2004 with Greens Functions  
179 modeled in the reference frame of CM (center of the mass of the total Earth system) to  
180 maintain theoretical consistency and adherence to current IERS conventions [Hao et al., 2016;  
181 Fu et al., 2012], but atmospheric pressure loading or any other loading variations (non-tidal  
182 ocean loading) with periods > 1 day were not removed. In order to focus on the seasonal and  
183 trend feature over the entire observation time, we first smoothed the data to reduce large  
184 scatter before using a 3-month-wide moving window filter to remove the short-period terms.

185

186 Due to the coseismic displacement of the 2011 Mw9.0 Tohoku earthquake, we estimated and  
187 removed offsets (i.e., using the differences of the average values of seven days between  
188 before and after earthquake to obtain the coseismic displacement) at those times for the  
189 vertical time series of GPS stations at Eastern China. Wang et al. [2011] study results reveal  
190 that the coseismic horizontal displacements induced by the earthquake are at the level of  
191 millimeters to centimeters in North and Northeast China, with a maximum of 35 mm, but the  
192 vertical coseismic and postseismic displacements are too small to be detected. In order to  
193 maintain consistency with the GIA effects present in the GRACE solutions, we remove GIA  
194 effects for all GPS stations using Stokes coefficients ( $l=100$ ) results computed by A et al.  
195 [2013], which used the ICE5G ice history and VM2 viscosity profile [Peltier et al., 2004].

196

197 Figure 3a shows the time series (2003-2012) of daily solutions for IGS GPS sites BJFS,  
198 ZHNZ, BJSH, JIXN and TAIN. The long-term linear trends are mainly dominated by surface



199 mass loading and tectonic processes, and the GPS time series shows significant seasonal  
200 variations. The peak-to-peak seasonal amplitude can be seen to be more than 20 mm which  
201 reflects the strong seasonal mass changes in the NCP. The GRACE data from CSR uses model  
202 output to remove the gravitational effects of atmospheric and oceanic mass variability from  
203 the satellite data before constructing monthly gravity field solutions. In order to compare the  
204 displacement from GPS with GRACE, the effects of atmospheric and non-tidal oceanic  
205 loading on the GPS coordinates needed to be removed. Displacements due to atmospheric  
206 loading were calculated using data and programs developed by the GGFC (Global  
207 Geophysical Fluid Center) (T. van Dam, NCEP Derived 6 hourly, global surface  
208 displacements at  $2.5^\circ \times 2.5^\circ$  spacing, <http://geophy.uni.lu/ncep-loading.html>, 2010). These  
209 utilized the NCEP (National Center of Environmental Protection) reanalysis surface pressure  
210 data set. The 12-hour sampling model, ECCO (Estimating the Circulation & Climate of the  
211 Ocean, <http://www.ecco-group.org/>), is used to compute the surface displacement driven by  
212 non-tidal ocean effects and its spatial resolution is  $1^\circ \times 0.3\text{--}1.0^\circ$ , i.e., 1 degree longitude (zonal)  
213 interval and 0.3 to 1.0 degree in latitude (meridian) intervals from equator to high latitude. An  
214 example of the effects of the non-tidal ocean and atmospheric loading in the GPS and  
215 GRACE data is provided in the supporting information (Figure S1).  
216  
217 The displacements caused by atmospheric pressure and non-tidal ocean loading mainly show  
218 seasonal fluctuations and no obvious long-term trend during GPS observation (e.g., time  
219 series of height from atmospheric and non-tidal ocean loading at IGS sites in Figure 3b). The  
220 annual amplitude is 4.0–4.6 mm and 0.24–0.42 mm for the atmospheric and non-tidal ocean



221 loading effects, respectively, while the semi-annual amplitude is about 0.3 mm and 0.03 mm,  
222 respectively. But the phases between the atmospheric and non-tidal ocean loading effects have  
223 more apparent difference. The results of the seasonal amplitudes and phase fits of vertical  
224 displacements, derived by GRACE and GPS for IGS stations between before and after  
225 corrected atmospheric and non-tidal ocean, are summarized in Table S1 in the supporting  
226 information.

227

### 228 **2.3 Elastic Displacements Due to Mass Loads**

229 GRACE Stokes coefficients [Wahr et al., 1998] and load Love numbers [Farrell, 1972] can be  
230 used to estimate the displacement effects in three components (Up, North and East) caused by  
231 mass load changes. The mathematical relationships [Kusche and Schrama, 2005; van Dam et  
232 al., 2007] between the radial surface displacement (Up or Height) and the Stokes coefficients  
233 of mass is:

$$234 \Delta h = dr(\theta, \phi) = R \sum_{l=1}^{N_{\max}} \sum_{m=0}^l \tilde{P}_{l,m}(\cos \theta) \cdot (C_{lm} \cos(m\phi) + S_{lm} \sin(m\phi)) \frac{h_l}{1+k_l} \quad (1)$$

235 where  $\Delta h$  is the displacement of the Earth's surface in the radial direction at latitude  $\theta$  (theta)  
236 and eastward longitude  $\phi$  (phi);  $N_{\max}=60$ ,  $R$  is the Earth's radius;  $\tilde{P}_{l,m}$  is fully normalized  
237 Legendre functions for degree  $l$  and order  $m$ ;  $C_{lm}$  and  $S_{lm}$  are time variable components of the  
238 ( $l,m$ ) Stokes coefficients for some month; and  $h_l$ ,  $k_l$  and  $l_l$  are the three degree dependent load  
239 Love numbers which are functions of Earth's elastic property. In this equation we adopted the  
240 load Love numbers provided by Han and Wahr [1995].

241

242 Similarly, horizontal displacements (North and East) can be calculated using the following



243 equations:

$$244 \quad \Delta n = dr(\theta, \phi) = -R \sum_{l=1}^{N_{\max}} \sum_{m=0}^l \frac{\partial}{\partial \theta} \tilde{P}_{l,m}(\cos \theta) \cdot (C_{lm} \cos(m\phi) + S_{lm} \sin(m\phi)) \frac{l_l}{1+k_l}, \quad (2)$$

$$245 \quad \Delta e = dr(\theta, \phi) = \frac{R}{\sin \theta} \sum_{l=1}^{N_{\max}} \sum_{m=0}^l \tilde{P}_{l,m}(\cos \theta) \cdot m(-C_{lm} \sin(m\phi) + S_{lm} \cos(m\phi)) \frac{l_l}{1+k_l}, \quad (3)$$

246 where  $\Delta n$  and  $\Delta e$  are north and east components of the displacement, respectively, with both  
247 having positive values when the crust moves towards the north and east, respectively. As is  
248 mentioned in Section 2.1 above, in order to be consistently comparable to the GPS time series,  
249 we corrected the degree-1 components to GRACE-derived mass variations, using Stokes  
250 coefficients derived by Swenson et al. [2008]. With corresponding to degree-1 contribution to  
251 vertical displacement, the value of load Love numbers of the degree-1 in the CF frame should  
252 be computed by using equation (23) in Blewitt [2003].

253

254 Figure 4 shows an example (site BJFS, JIXN, TAIN and ZHNZ) of the GRACE-derived  
255 vertical (Figure 4c) and horizontal displacements (Figure 4a and 4b) before and after  
256 destriping. It can clearly be seen that the maximal amplitude of vertical displacement is  
257 several order of magnitude higher than horizontal displacements. In addition, the calculated  
258 results using the monthly GRACE model data after destriping show that the effects of TWS  
259 (soil moisture, etc.) on surface displacements are seasonal variations and long-term changes  
260 on vertical and horizontal components. As most of the stations are located in areas of TWS  
261 loss in the NCP (see sites location in Figure 2), the fact is that the motion is upward (see the  
262 positive trend of GRACE-derived vertical in Table 1) during this event (if a load is removed,  
263 the site uplifts and moves away from the load [Wahr et al., 2013]). Identified horizontal



264 displacements are important as they constrain the location of load changes [Wahr et al., 2013;  
265 Wang et al., 2014]. The displacement of the ZHNZ site is upwards and to the south (see the  
266 negative trend of the ZHNZ north component in Figure 4a) due to the mass loss almost due  
267 north of the site. Correspondingly, the displacement of the TAIN site is upwards and to the  
268 southeast (see the negative trend of the north component and the positive trend of the east  
269 component of the TAIN site in Figure 4a and 4b) caused by the mass loss located to the  
270 northwest of the site, based on the use of GPS horizontals for loading studies from Wahr et al.  
271 [2013].

272

### 273 **3. GRACE-derived Seasonal Variations and Comparison with GPS Measurements**

274 Using equation (1) and GRACE-derived Stokes coefficients, the vertical displacements at the  
275 GPS sites in the NCP and its surrounding region can be calculated. To focus on these changes,  
276 GRACE-derived vertical displacements were computed by fitting a model with a linear trend  
277 and annual periodic terms using Least-Squares method over the entire 11 year time span, for  
278 comparison to the seasonal variations observed by GPS (Table 1). Figure 5 shows time series  
279 of vertical displacements for GPS sites of IGS stations (BJFS, BJSN, JIXN, TAIN and ZHNZ).  
280 The fitting results show the GRACE-derived (without ADO1B) peak-to-peak annual  
281 amplitudes can be more than 2 mm, and the semi-annual amplitude are also visible at these  
282 five GPS sites. This reflects the climate-derived seasonal hydrological fluctuations in the  
283 NCP.

284

285 Compared with GRACE results mainly due to the mass change in seasonal and long-term



286 linear period, all GPS time series show significant seasonal and long-term trends which are  
287 mainly dominated by tectonic and hydrological process. The fitting results (after  
288 Least-Squares fitting) show the peak-to-peak vertical seasonal displacements from GPS time  
289 series to be larger than GRACE-derived results at those GPS sites, and the peak-to-peak  
290 seasonal amplitude changes between 5 mm and 6 mm (Table 1). The results of the comparison  
291 between GPS and GRACE-derived seasonal height variations at 24 GPS sites from  
292 CMONOC can be seen in Figure S3 in the supporting information. For all the selected GPS  
293 sites, the annual component is more dominant than the semi-annual one. The peak-to-peak  
294 annual amplitude is 1.2~6.3 mm and 1.0~2.2 mm for the GPS and GRACE solutions,  
295 respectively, while the semi-annual amplitude is about 1/2~1/3 times of that in annual  
296 amplitude. These more consistent seasonal variations of GRACE and GPS height time series  
297 reflect the climate-derived seasonal hydrologic process, i.e., heavy monsoonal precipitation in  
298 the late summer months result in mass loads increase (the maximum negative of vertical  
299 amplitude) and largely pumped for agricultural usage in late spring months cause mass loads  
300 decrease (the maximum positive of vertical amplitude). We observe the fact that the amplitude  
301 of GPS is relatively larger than that of GRACE, it is not only exists in the IGS stations, but in  
302 almost all stations except SXGX (Table 1). This indicates that GPS has a strong sensitivity for  
303 local surface loading. By contrast, because the spatial resolution of GRACE data is limited to  
304 approximately 300 km ( $N_{max}=60$ ), GRACE-derived results are mainly constrained by large  
305 scale areas. This means that GRACE-derived vertical displacements show a small difference  
306 between stations due to the results are averaged over scales of several hundred km or more.  
307



308 As is mentioned above, the cause of the difference between our results and Liu's work [Liu et  
309 al., 2014] is we removed atmospheric and non-tidal ocean loading effects while they did not.  
310 However, we found that the amplitude of GPS after removed atmospheric and non-tidal ocean  
311 loading effects, is still greater than the GRACE while we added the AOD1B de-aliasing  
312 model to the GRACE solutions (i.e., no atmospheric and non-tidal ocean corrected, please see  
313 the Table S1 in the supporting information). The most obvious difference between our results  
314 and Liu's work [Liu et al., 2014] is that they adopt the load Love numbers from Guo et al.  
315 [2004] to transform these coefficients into vertical surface displacement estimates. We check  
316 the two results of Love numbers (ocean-load and atmospheric pressure-load) from Guo et al.  
317 [2004], there are significant differences between ocean-load and atmospheric pressure-load  
318 Love numbers. Meanwhile, we compared  $k_n$  Love numbers from Guo et al. [2004] (Liu et al.'s  
319 work) and  $k_n$  Love numbers from Han and Wahr [1995] (our work) with the  $k_n$  Love numbers  
320 used in ADO1B products [Farrell, 1972], respectively. The different Love numbers have  
321 caused the amplitude of the same station from Liu's GRACE-derived vertical displacements  
322 much more than GPS and our GRACE results, due to  $k_n$  from atmospheric pressure-load Love  
323 numbers [Guo et al., 2004] significantly larger than Love numbers from Han and Wahr [1995]  
324 and Farrell [1972]. The detailed analysis of the different Love numbers from Guo et al. [2004],  
325 Han and Wahr [1995] and Farrell [1972], please see the Section S1 in the supporting  
326 information  
327  
328 Next, we compare GPS observed and GRACE-derived seasonal height variations. The  
329 estimated annual amplitudes and initial phases derived from GPS (grey vector) and GRACE



330 (red vector) are shown in Figure 6. We find that there are many sites where the signals  
331 disagree in both amplitude and phase. The annual amplitudes and phases from  
332 GRACE-derived results are much more spatially coherent than those determined from the  
333 GPS heights. Because GRACE solutions truncate to  $l_{max}=60$  and the Gaussian filtering was  
334 used to lead to so smooth out concentrated loads. The phases of the GRACE data show that  
335 the annual signal peaks (summer monsoon) basic between September and October and  
336 indicate that the maximum load occurs in this two months. But there are several sites where  
337 the GRACE signals disagree in phase with GPS data, which the annual signal peaks sometime  
338 between August and September. The five signals of sites in the northwest foothills region of  
339 NCP agree in phase, while annual amplitudes from GRACE are significantly less than GPS,  
340 e.g., NMTK, NMZL, HEYY, HEZJ and HECC. The cause of mostly phase inconsistency may  
341 be the different spatial resolution of GRACE compared to GPS. That is, GPS measurements  
342 can sense the difference between loads very near the site, and loads a bit further away, but  
343 GRACE with wavelengths on the order of 300 km reflects this variation at a monthly scale.  
344 Another important reason is that a one-month sampling of GRACE means a phase sampling  
345 of  $30^\circ$ , while a one-day sampling of GPS means a phase sampling of  $\sim 1^\circ$ , the different  
346 temporal sampling rate caused the inconsistent phase between GRACE and GPS.  
347  
348 With the purpose of quantitatively evaluating the consistency between GPS and GRACE, we  
349 remove GRACE-derived seasonal displacement from GPS observed detrended height time  
350 series to compute the reductions of Weighted Root Mean Squares (WRMS) based on the  
351 equation (2) in van Dam et al. [2007]. Correlation between GPS and GRACE derived



352 seasonal variations and WRMS reduction ratio of remove GRACE-derived seasonal  
353 displacement from GPS observed detrended height time series, please see the Table S4 in the  
354 supporting information for details. All the selected sites show high correlation (85%–99%,  
355 without TJBH site) when atmospheric and non-tidal ocean effects was not removed. Our  
356 correlation results of IGS stations (BJFS, BJSN, JIXN, TAIN and ZHNZ) are consistent with  
357 Liu's work [Liu et al., 2014], indicating that the seasonal variations might come from the  
358 same geophysical process. The WRMS residual reduction ratio for all the stations ranged  
359 from 19% to 85%, which is better than Liu's work [Liu et al., 2014]. However, the correlation  
360 and WRMS reduction between GPS and GRACE are weak when atmospheric and non-tidal  
361 ocean effects was removed, with the average correlation and WRMS reduction reduce to 75.6%  
362 and 28.9%, respectively. This is mainly because the seasonal hydrologic process is major  
363 contributors to seasonal changes, and different stations are greatly influenced by the  
364 surrounding hydrological process. By contrast, the seasonal amplitudes and phases from  
365 GRACE results are much more spatially coherent than those determined from the GPS  
366 heights, caused by the different spatial resolution between them. In addition, we also attempt  
367 to calculate GRACE-derived horizontal displacement using equation (2) and (3), and compare  
368 it with the GPS measurements. An example (five IGS sites) of the comparison between  
369 GRACE-derived and GPS observed horizontal displacements were presented to demonstrate  
370 the correlation of seasonal horizontal variation caused by surface hydrological load. Please  
371 see the Figure S4 in the supporting information.

372

373 **4. Long-Term Uplift Caused by TWS Loss**



374 To estimate TWS changes averaged over the NCP, an averaging kernel based on weighted  
375 Gaussian convolution to construct monthly time series from GRACE Stokes coefficients  
376 described by equation (5) of Wahr et al. [2014] was used. This method extends the averaging  
377 kernel convolution approach [Swenson and Wahr, 2002] by allowing for nonuniform  
378 weighting during the convolution. We took the NCP “basin function” from the China  
379 provincial boundary grid points and we convolved with a 250 km Gaussian smoothing. We  
380 then applied this averaging kernel to GRACE Stokes coefficients to obtain a TWS time series  
381 for NCP (Figure 7). The results identified a continuous decrease in TWS from 2004 to 2009;  
382 the rate of this decrease slowed towards the end of 2009. The rate of TWS loss obtained by  
383 this analysis was 1.62 cm/yr from 2003 to 2009 and 1.23 cm/yr from 2003 to 2012 (Table 2).  
384  
385 The estimated results for the time series analysis also include some contributions outside the  
386 NCP due to the finite number of harmonic degrees in the GRACE solution (e.g.,  $l_{max}=60$  for  
387 CSR solutions). The average kernel in our study is also not an exact unity cover for the entire  
388 NCP area; these two factors result in under or overestimation of the true TWS time series  
389 signal. To estimate this “leakage in” signal, a scaling factor method was used to restore the  
390 amplitude-damped TWS time series. This method, as described by Wahr et al. [2014], requires  
391 the construction of a set of simulated Stokes coefficients which represents the signal from a  
392 uniformly distributed 1 cm water depth change over the NCP. This estimates a water  
393 volume=3.6626 km<sup>3</sup> based on the overall area of “basin function” (i.e., 366260 km<sup>2</sup>). By  
394 applying our GRACE analysis procedure to these simulated Stokes coefficients, we can infer  
395 an average water thickness change equal to 0.47 cm for the NCP. Each monthly GRACE



396 estimate of NCP water thickness is then multiplied by a scaling factor=1 (cm)/0.47 (cm) to  
397 obtain variations in the total water thickness per area of the NCP. Multiplying the monthly  
398 GRACE estimates of NCP water thickness by a scaling factor=3.6626 (km<sup>3</sup>)/0.47 (cm)  
399 provides a mass change of the NCP. Table 2 shows the rate of GRACE-derived TWS loss  
400 (after multiplying by the scaling factor) in the NCP was 3.39 cm/yr from 2003 to 2009; this is  
401 equivalent to a volume of 12.42 km<sup>3</sup>/yr. For a 10-year time span, the rate was 2.57 cm/yr,  
402 which is equivalent to a volume of 9.41 km<sup>3</sup>/yr.

403

404 Loading or unloading of the crust from surface mass changes will cause the crust to subside or  
405 uplift with different amplitudes. These displacements depend on the amplitude of the load and  
406 the distance between the load and the observation point [Farrell, 1972]. On this basis, we used  
407 GRACE-derived vertical displacements (the method of elastic displacements due to mass  
408 loads described by Section 2.3) to evaluate TWS loss contributions for the evident crustal  
409 uplift in the GPS measurements. Time series of monthly predicted vertical surface  
410 displacements from GRACE for 25 GPS sites in the NCP were plotted (Figure 8a). The fitting  
411 results (after Least-Squares fitting) show the trend rate of GRACE-derived vertical  
412 displacements for the whole region at the 0.37–0.95 mm/yr level from 2004 to 2009, but the  
413 rate of change direction is inconsistent in different GPS stations at -0.40–0.51 mm/yr level  
414 from 2010 to 2013 (Table 1). The smoothed results indicate a rising trend from 2004 to 2012  
415 (Figure 8a) which represented the TWS loss in the observation time span. Figure 8a also  
416 clearly shows mass anomaly due to TWS changes in the vertical component, e.g., a notable  
417 negative peak from 2003 to 2005 and subsidence in 2012 (grey background in Figure 8a).



418 These GRACE-derived long-term height fluctuations mainly include variations in the storage  
419 of natural surface water: high storage in wet years and low storage in dry years [Tang et al.,  
420 2013], which can be modeled using land surface model output such as those provided by the  
421 GLDAS [Rodell et al., 2004]. We clearly see that these fluctuations are almost erased by  
422 removing the modeled soil moisture (SM) of GLDAS/Noah, and the obvious uplift are  
423 presented in the decomposition of the signal (Figure 8b), which is mainly because the  
424 contributions from groundwater depletion in the NCP (please see the section 5.1 for discuss in  
425 details).

426

427 **5. Discussion**

428 **5.1 Groundwater Depletion Contributions to Long-Term Uplift**

429 The GRACE-derived vertical displacements are also the effect of mass loading sensitive to  
430 water at all depths: surface water storage, soil moisture, snow and groundwater, including  
431 anthropogenic effects (i.e., groundwater withdrawal, inter-basin diversion, reservoir and coal  
432 transport). To isolate the groundwater contributions, the Noah version of GLDAS which  
433 possesses monthly intervals and spatial resolution of 1.0 degrees [Rodell et al., 2004] was  
434 used to subtract monthly water storage estimates predicted by land surface models. GLDAS  
435 generates a series of land surface forcing (e.g., precipitation, surface meteorology and  
436 radiation), state (e.g., soil moisture and temperature, and snow), and flux (e.g., evaporation  
437 and sensible heat flux) data simulated by land surface models. The GLDAS/Noah model can  
438 provide values of snow, vegetation and all soil moisture layers, but it does not include  
439 anthropogenic and climate-driven groundwater depletion. So groundwater contributions



440 retained in heights time series when GRACE-derived vertical displacements subtracting

441 GLDAS/Noah effects.

442

443 Figure 8b shows the GRACE-derived height amplitudes after using output from the

444 GLDAS/Noah hydrology model to remove the continental water storage signal. The

445 calculated results show that the contributions of other types of TWS effects (except

446 groundwater) on the surface are small relative to groundwater depletion, and those loads

447 mainly effects on the amplitudes of seasonal displacement with no obvious long-term trend.

448 Compare the seasonal amplitudes, phases and trend fit of vertical displacements between

449 before and after remove GLDAS/Noah effects from GRACE-derived displacement, please see

450 the Table S4 in the supporting information.

451

452 For the results described above, after the subtraction of the GLDAS/Noah contributions,

453 GRACE-derived heights largely reflect loading effects from the groundwater (natural and

454 anthropogenic factors) and anthropogenic contributions. The anthropogenic impact on mass

455 change was investigated by Tang et al. [2013] for the effect of inter-basin diversion, reservoir

456 and coal transport distribution on the GRACE-derived estimates of groundwater depletion in

457 the NCP. Results from their investigation showed that the trend of anthropogenic

458 contributions was equivalent to 4.83 mm/yr water thickness (described by equations in Table

459 2 of Tang et al. [2013]) during 2003-2011 for the whole NCP. This means that there was a

460 large groundwater depletion contribution for the GRACE-derived vertical displacements in

461 long-term uplift. Investigating groundwater withdrawal due to anthropogenic activities



462 (drinking water extraction, agricultural irrigation and industrial manufacturing) should be of  
463 high importance because precipitation data for this area (provided by the China  
464 Meteorological Data Sharing Service System, available at <http://cdc.nmic.cn/home.do>)  
465 indicated no long-term droughts during the GRACE observation period of 2003-2011.

466

## 467 **5.2 Removing Hydrological Loading Displacement from GPS Using GRACE Data**

468 Coordinate variations measured by GPS stations, principally for the vertical component, have  
469 been used to investigate global [Dong et al., 2002] and local [Grapenthin et al., 2006] tectonic  
470 activity, as well as seasonal displacement modes for constraining estimates of continental,  
471 atmospheric and ocean water storage. Some previous studies [e.g., Fu et al., 2012] have  
472 focused on the vertical component of crustal motion with relying on the accurate  
473 interpretation of GPS motion in terms of surface stress or tectonic movement. Thus, the  
474 displacement signal from surface mass loading is a source of noise [van Dam et al., 2007].  
475 For these applications, they would like to obtain reliable loading models or even surface mass  
476 observations, which can be used to reduce the environmental loading contributions to the GPS  
477 observations. In this study, we also attempt to separate tectonic and hydrological effect using  
478 GRACE-derived hydrological vertical rates. As mentioned in the Section 3, the good seasonal  
479 correlation between GRACE and GPS signals indicates that the long-term uplifts revealed by  
480 GRACE detections are probably true and mixed in the GPS measurements.

481

482 Figure 9 shows results for individual GPS time series. Crustal subsidence or uplift due to  
483 vertical tectonic motion and TWS changes in the studied period are clearly evident in the



484 vertical component shown in most of the GPS stations; In fact, the analysis in the five IGS  
485 GPS stations (BJFS, BJSN, JIXN, TAIN and ZHNZ) suggests that the GPS vertical time  
486 series can be described by two different rates around 2010, due to a continuous decrease in  
487 TWS from 2004 until 2009; towards the end of 2009 the rate of this decrease slowed and rate  
488 started to rise since 2010 (please see Figure 6). Thus, we divided it into two periods when  
489 fitting GPS and GRACE trend for these five stations (Figure 9a). GPS trend changes indicate  
490 an overall uplift for the whole region at the 0.04–1.47 mm/yr level from 2004 to 2009, but the  
491 rate of change direction is inconsistent in different GPS stations at -0.94–2.55 mm/yr level  
492 from 2010 to 2013 (Table 1).

493

494 In addition, the long-term trend rate is different in different areas from 2010 to 2013 (Figure  
495 9b). For example, the trend rate from GPS measurements shows the uplift in western NCP  
496 (Shanxi-SX, and some of Hebei-HE stations), but opposite trends in the central and eastern  
497 plain of NCP (Beijing-BJ, Tianjin-TJ and some of Hebei-HE stations). The groundwater  
498 depletion which occurs in the shallow unconfined aquifers in Piedmont Plain leads to the  
499 loading uplift effect from mass loss. But groundwater depletion occurs in the deep confined  
500 aquifers in the central and eastern plain of NCP, which causes serious ground subsidence,  
501 rather than ground uplift caused by groundwater loss.

502

503 It is also possible that some GPS signals could be a result of loading from changes in the  
504 distribution of water stored in the surface and ground around the GPS surrounding region. To  
505 remove those contributions, Stokes coefficients output from the GRACE model were used to



506 compute crustal motion at the NCP (Figure 8a), and then transform the monthly results into  
507 daily resolution data using a spline interpolation. In addition, GRACE solutions are corrected  
508 for GIA while GPS ones are not. Here Stokes coefficients results from A et al. [2013] were  
509 used to remove GIA effects from GPS measurements, which is about 0.2–0.4 mm/year in the  
510 land areas of China and 0.28–0.33 mm/year in the NCP (Please see the Figure S5 and Table  
511 S4 in the supporting information).

512

513 We compute the GRACE-derived long-term uplift for all continuous GPS sites used in this  
514 paper. The results indicate an overall uplift for the NCP region. Then we remove this TWS  
515 induced uplift from GPS actual observed vertical rates to derive the corrected vertical  
516 velocities. Figure 10 divided the time into two periods (2004–2009 and 2010–2013) to  
517 indicate an overall long-term trend before (gray arrow) and after (red arrow) removing  
518 hydrological loading displacement for the whole region. Secular displacement results between  
519 2004 and 2009 show that loading displacement due to the TWS loss reduce the uplift rate of  
520 GPS to some extent, and groundwater exploitation was the main contributor to crustal uplift  
521 caused by TWS loss in the NCP (BJFS, BJSN and JIXN in the Figure 10a). However, studies  
522 indicate that groundwater withdrawal produces localized subsidence which can be largely  
523 relative to tectonic displacement [Bawden et al., 2001]. Therefore, in this study, more  
524 attention was paid to land subsidence due to groundwater loss.

525

### 526 **5.3 Land subsidence in the central and eastern of NCP**

527 Land subsidence has been commonly observed in the NCP, and has become the main factor



528 that impacts regional sustainable economic and social development [Guo et al., 2015]. Over  
529 the past years, the scope and magnitude of land subsidence has expanded. In this study, we  
530 used GPS sites to obtain time series of land subsidence evolution characteristics. The trend  
531 rates from GPS sites, after removing the rates from GRACE-derived long-term uplift and GIA  
532 effects can be seen in Figure 10b (the gray background areas in the dashed white box) to  
533 reflect the rate of land subsidence from 2010 to 2013, which is because the groundwater  
534 exploitation in the deep confined aquifers has a more serious impact on land subsidence [Guo  
535 et al., 2015]. The results show that Tianjin becomes the most serious subsidence area, e.g., in  
536 the Tanggu and Hangu district (TJBH), with an average subsidence of ~14 mm/yr after 2010;  
537 In Wuqing district (TJWQ), recent subsidence averaged ~43 mm/yr. Because the Cangxian  
538 district (HECX) is close in proximity to the Jinghai region of Tijian, the sedimentation rate of  
539 ~20 mm/yr can represent the subsidence trend of southwest Tianjin. However, the difference  
540 of spatial distribution of land subsidence is large in Tianjin, and uneven settlement  
541 characteristics are obvious. For example, the southwest and western areas of Tianjin are the  
542 most serious areas, and the trend of land subsidence exists in the northward but the amplitude  
543 is small relative to the southwest and western areas, i.e., (JIXN site shows a small negative  
544 trend (~-0.6 mm/yr). The cause for subsidence in the Tianjin area is linked to over  
545 exploitation of groundwater, an issue that has not been effectively controlled resulting in  
546 rapidly developing land subsidence in the suburbs in recent years [Yi et al., 2011].

547

548 In the central and eastern region of NCP, where disastrous land subsidence has also occurred  
549 in Beijing and cities in central of Hebei province and the northeast of Shandong province, for



550 instance, large subsidence zone in Hebei province has formed from north to south, where start  
551 from the western region of Beijing (BJFS, BJSH and BJJYQ station), via the eastern region of  
552 Xingtai and Handan (HELY station), extend to the northern of Hebi (HAHB station belong to  
553 Henan province).

554

555 However, results from our investigation show that the center of land subsidence does not  
556 completely overlap the TWS loss contributions (see the secular trend maps of the TWS  
557 changes of NCP in Figure 2). The uplift still exists even when we removed the rates from  
558 GRACE-derived and GIA effects in the piedmont of Taihang Mountains and the western part  
559 of NCP (Shanxi province), where the groundwater depletion occurs in the shallow unconfined  
560 aquifers have not led to a large area of subsidence. The reason for this difference with the  
561 western region of NCP is that crustal uplift is mainly controlled by tectonic movement, which  
562 is the orogenic belt and plateau area in western of the Taihang Mountains basic in the uplift.

563 In our results, most of the corrected vertical velocities at GPS stations, especially in the  
564 central and eastern region of NCP, agree with the previous study results, i.e., combining with  
565 mobile and continuous GPS observation [Zhao et al., 2014] and using GPS stations from  
566 GNSS and leveling data [MLR, 2015], The results of vertical crust movement in the NCP  
567 from the previous study, please see the Figure S6 in the supporting information.

568

## 569 **6. Conclusions**

570 Temporal variations in the geographic distribution of surface mass (continental water, ocean  
571 mass and atmospheric mass) can lead to displacement of the Earth's surface. Due to excessive



572 exploitation of groundwater resources the NCP area has become susceptible to land  
573 subsidence, and it has become one of the most affected areas in the world. Calculating the  
574 loading displacement can explain the natural displacement phenomenon, and it presents new  
575 insight into the dynamics of land subsidence.

576

577 Traditional displacement observation has space limitations. Based on the elastic displacement  
578 of the Earth's crust by surface loadings, this study combined GRACE and GPS data to  
579 investigate vertical displacements in the NCP area. GRACE data was used to model vertical  
580 displacements due to changes in hydrological loads. The results showed both GPS and  
581 GRACE data to observe strong seasonal variations. Comparisons between the observed GPS  
582 seasonal vertical displacement and GRACE-derived seasonal displacement demonstrated that  
583 a consistent physical mechanism is responsible for TWS changes, i.e., the seasonal  
584 hydroospheric mass movements due to climate variability cause periodic displacements of the  
585 lithosphere.

586

587 As well as the significant seasonal characteristics, GRACE also exhibited a long-term mass  
588 loss in this region; the rate of GRACE-derived TWS loss (after multiplying by the scaling  
589 factor) in the NCP was 3.39 cm/yr from 2003 to 2009, which is equivalent to a volume of  
590  $12.42 \text{ km}^3/\text{yr}$ . The rate was 2.57 cm/yr from 2003 to 2012, equivalent to a volume of 9.41  
591  $\text{km}^3/\text{yr}$ . The TWS loss was principally due to groundwater depletion in the NCP. We  
592 calculated that the consequent trend rate caused by the load mass change using GRACE data  
593 and removed this hydrological effect from observed GPS vertical rates. Secular displacement



594 results showed that TWS losses reduced loading displacement to some extent, but the trend  
595 rates disagree due to the difference of spatial distribution with anthropogenic depletion of  
596 TWS in the NCP.

597

598 Particularly, land subsidence has been affecting the central and eastern region of NCP,  
599 especially in Tianjin for the past years. Over-pumping of groundwater is the main cause of  
600 land subsidence which has led to comprehensive detrimental effects on the society, the  
601 economy and the natural environment. The impact of groundwater exploitation in different  
602 aquifer systems and active faults in the different regions on land subsidence needs to be  
603 analyzed in future investigations. For example, using GRACE to remove mass loading signals  
604 from a GPS record requires either confidence that there is no concentrated load signal very  
605 near the site, or a scaling factor based on a reliable model of the mass change (the  
606 groundwater depletion rate estimated from monitoring well stations) pattern around the site.

607

608 **Acknowledgments.** The GPS data of CMONOC and IGS were made by First Crust  
609 Monitoring and Application Center, China Earthquake Administration  
610 (<http://www.eqdsc.com/data/pgv-sjxl.htm>). We also thank the Center of Space Research (CSR)  
611 teams for their online accessible GRACE solutions  
612 (<ftp://podaac.jpl.nasa.gov/allData/grace/L2/CSR/RL05/>) and the GLDAS/Noah model data  
613 provided by the NASA Goddard Earth Sciences Data and Information Services Center  
614 (<http://disc.sci.gsfc.nasa.gov/>). This work was initiated while L. Wang was visiting Prof. John  
615 Wahr at the Department of Physics, University of Colorado at Boulder. We are grateful to Prof.



616 John Wahr for his helpful suggestions, including estimating the TWS changes averaged over  
617 the NCP using averaging kernel method and loading responses due to water change using  
618 GRACE Stokes coefficients to calculate the elastic displacement. This work is supported by  
619 the National Natural Science Foundation of China (NSFC) (Grant No. 41504065), China  
620 Postdoctoral Science Foundation funded project (Grant No. 2014T70753), the China  
621 University of Geosciences (CUG) Hubei Subsurface Multi-scale Imaging Lab (Grant No.  
622 SMIL-2014-09) and Hubei province natural science foundation of China (Grant No.  
623 2014CFB170).

624

## 625 **References**

626 A, G., Wahr, J., Zhong, S., 2013. Computations of the viscoelastic response of a 3-D  
627 compressible earth to surface loading: An application to glacial isostatic adjustment in  
628 Antarctica and Canada. *Geophys. J. Int.* 192, 557–572. doi: 10.1093/gji/ggs030.

629 Altamimi, X., Collilieux, X., Metivier, L., 2011. ITRF2008: An improved solution of the  
630 International Terrestrial Reference Frame. *J. Geod.* 85(8), 457–473. doi:  
631 10.1007/s00190-011-0444-4.

632 Bawden, G.W., Thatcher, W., Stein, R.S., Wicks, C., Hudnut, K., Peltzer, G., 2001. Tectonic  
633 contraction across Los Angeles after removal of groundwater pumping effects. *Nature* 412,  
634 812–815. doi: 10.1038/35090558.

635 Bevis, M., Alsdorf, D., Kendrick, E., Fortes, L.P., Forsberg, B., Smalley Jr., R., Becker, J.,  
636 2005. Seasonal fluctuations in the mass of the Amazon River system and Earth's elastic  
637 response. *Geophys. Res. Lett.* 32, L16308. doi: 10.1029/2005GL023491.



638 Blewitt, G., 2003. Self-consistency in reference frames, geocenter definition, and surface  
639 loading of the solid Earth. *J. Geophys. Res.*, 108(B2). doi: 10.1029/2002JB002082.

640 Boehm, J., Heinkelmann, R., Schuh, H., 2007. Short note: A global model of pressure and  
641 temperature for geodetic applications. *J. Geod.* 81, 679–683. doi:  
642 10.1007/s00190-007-0135-3.

643 Chao, B.F., Wu, Y., Li, Y., 2008. Impact of artificial reservoir water impoundment on global  
644 sea level. *Science* 320, 212–214. doi: 10.1126/science.1154580.

645 Cheng, M.K., Tapley, B.D., Ries, J.C., 2013. Deceleration in the earth's oblateness. *J.*  
646 *Geophys. Res.* 118, 1–8. doi: 10.1002/jgrb.50058.

647 Döll, P., 2009. Vulnerability to the impact of climate change on renewable groundwater  
648 resources: a global-scale assessment. *Environ. Res. Lett.* 4, 036006. doi:  
649 10.1088/1748-9326/4/3/035006.

650 Döll, P., Kaspar, F., Lehner, B., 2003. A global hydrological model for deriving water  
651 availability indicators: Model tuning and validation. *J. Hydrol.* 270, 105–134.

652 Dong, D., Fang, P., Bock, Y., Cheng, M.K., Miyazaki, S., 2002. Anatomy of apparent seasonal  
653 variations from GPS-derived site position time series. *J. Geophys. Res.* 107(B4), 2075. doi:  
654 10.1029/2001JB000573.

655 Farrell, W.E., 1972. Deformation of the Earth by surface loadings. *Rev. Geophys. Space Phys.*  
656 10, 761–797. doi: 10.1029/RG010i003p00761.

657 Feng, W., Zhong, M., Lemoine, J.M., Biancale, R., Hsu, H.T., Xia, J., 2013. Evaluation of  
658 groundwater depletion in North China using the Gravity Recovery and Climate Experiment  
659 (GRACE) data and ground-based measurements. *Water Resour. Res.* 49, 2110–2118. doi:



660 10.1002/wrcr.20192.

661 Fu, Y., Argus, D.F., Freymueller, J.T., Heflin, M.B., 2013. Horizontal motion in elastic  
662 response to seasonal loading of rain water in the Amazon Basin and monsoon water in  
663 Southeast Asia observed by GPS and inferred from GRACE. *Geophys. Res. Lett.* 40. doi:  
664 10.1002/2013GL058093.

665 Fu, Y., Freymueller, J.T., 2012. Seasonal and long-term vertical deformation in the Nepal  
666 Himalaya constrained by GPS and GRACE measurements. *J. Geophys. Res.* 117, B03407. doi:  
667 10.1029/2011JB008925.

668 Fu, Y., Freymueller, J.T., and van Dam, T., 2012. The effect of using inconsistent ocean tidal  
669 loading models on GPS coordinate solutions. *J. Geod.*, 86(6), 409–421. doi:  
670 10.1007/s00190-011-0528-1.

671 Grapenthin, R., Sigmundsson, F., Geirsson, H., Árnadóttir, T., Pinel, V., 2006. Icelandic  
672 rhythmites: Annual modulation of land elevation and plate spreading by snow load. *Geophys.*  
673 *Res. Lett.* 33, L24305. doi: 10.1029/2006GL028081.

674 Guo, H., Zhang, Z., Cheng, G., Li, W., Li, T., Jiao, J. J., 2015. Groundwater-derived land  
675 subsidence in the north China plain. *Environ. Earth Sci.* 74, 1415–1427. doi:  
676 10.1007/s12665-015-4131-2.

677 Guo, J.Y., Li, Y.B., Huang, Y., Deng, H.T., Xu, S.Q., Ning, J.S., 2004. Green's Function of  
678 Earth's Deformation as a Result of Atmospheric Loading. *Geophys. J. Int.*, 159, 53–68. doi:  
679 10.1111/j.1365-246X.2004.02410.x.

680 Han, D., and Wahr, J., 1995. The viscoelastic relaxation of a realistically stratified Earth, and  
681 a further analysis of post-glacial rebound. *Geophys. J. Int.*, 120, 287–311.



682 Hao, M., Freymueller, J.T., Wang, Q.L., Cui, D.X., Qin, S.L., 2016. Vertical crustal movement  
683 around the southeastern Tibetan Plateau constrained by GPS and GRACE data. *Earth Planet.*  
684 *Sci. Lett.*, 437(5107), 1–8. doi: 10.1016/j.epsl.2015.12.038.

685 Heki, K., 2001. Seasonal modulation of interseismic strain buildup in north-eastern Japan  
686 driven by snow loads. *Science* 293, 89–92. doi: 10.1126/science.1061056.

687 Huang, Z., Pan, Y., Gong, H., Yeh, P.J.F., Li, X., Zhou, D., Zhao, W., 2015. Subregional-scale  
688 groundwater depletion detected by GRACE for both shallow and deep aquifers in North  
689 China Plain. *Geophys. Res. Lett.* 42, 1791–1799. doi: 10.1002/2014GL062498.

690 Joodaki, G., Wahr, J., Swenson, S., 2014. Estimating the human contribution to groundwater  
691 depletion in the Middle East, from GRACE data, land surface models, and well observations.  
692 *Water Resour. Res.* 50, 2679–2692. doi: 10.1002/2013WR014633.

693 Khan, S.A., Wahr, J., Bevis, M., Velicogna, I., Kendrick, E., 2010. Spread of ice mass loss  
694 into northwest Greenland observed by GRACE and GPS. *Geophys. Res. Lett.* 37, L06501. doi:  
695 10.1029/2010GL042460.

696 Kusche, J., Schrama, E.J.O., 2005. Surface mass redistribution inversion from global GPS  
697 deformation and Gravity Recovery and Climate Experiment (GRACE) gravity data. *J.*  
698 *Geophys. Res.* 110, B09409. doi: 10.1029/2004JB003556.

699 Liu, R.L., Li, J.C., Fok, H.S., Shum, C.K., Li, Z., 2014. Earth surface deformation in the  
700 North China Plain detected by joint analysis of GRACE and GPS data. *Sensors* 14,  
701 19861–19876. doi: 10.3390/s141019861.

702 Ministry of Land and Resources of China (MLR), 2015. Monitoring results of important  
703 geographical conditions in the Beijing-Tianjin-Hebei region, Ministry of Land and Res. of



704 China, Beijing. [Available at <http://www.mlr.gov.cn/>].

705 Moiwo, J.P., Tao, F., Lu, W., 2013. Analysis of satellite-based and in situ hydro-climatic data  
706 depicts water storage depletion in North China Region. *Hydrol. Process.* 27, 1011–1020. doi:  
707 10.1002/hyp.9276.

708 Nielsen, K., Khan, S.A., Spada, G., Wahr, J., Bevis, M., Liu, L., van Dam, T., 2013. Vertical  
709 and horizontal surface displacements near Jakobshavn Isbræ driven by melt-induced and  
710 dynamic ice loss. *J. Geophys. Res. Solid Earth* 118, 1837–1844. doi: 10.1002/jgrb.50145.

711 Oleson, K. W., et al., 2013. Technical description of version 4.5 of the Community Land  
712 Model (CLM), NCAR Tech. Note NCAR/TN-5031STR, 434 pp, National Center for  
713 Atmospheric Research, Boulder, Colorado.

714 Peltier, W.R., 2004. Global glacial isostasy and the surface of the ice-age earth: The ice-5G  
715 (VM2) model and GRACE. *Annu. Rev. Earth Planet. Sci.* 32, 111–149.

716 Rodell, M., et al., 2004. The global land data assimilation system. *Bull. Am. Meteorol. Soc.*  
717 85, 381–394. doi: 10.1175/BAMS-85-3-381.

718 Rodell, M., Velicogna, I., Famiglietti, J.S., 2009. Satellite-based estimates of groundwater  
719 depletion in India. *Nature* 460, 999–1002. doi: 10.1038/460789a.

720 Sauber, J., Plafker, G., Molnia, B.F., Bryant, M.A., 2000. Crustal deformation associated with  
721 glacial fluctuations in the eastern Chugach Mountains, Alaska. *J. Geophys. Res. Solid Earth*  
722 105(B4), 8055–8077. doi: 10.1029/1999JB900433.

723 Swenson, S., Chambers, D., Wahr, J., 2008. Estimating geocenter variations from a  
724 combination of GRACE and ocean model output. *J. Geophys. Res.* 113, B08410. doi:  
725 10.1029/2007JB005338.



726 Swenson, S., Wahr, J., 2002. Methods for inferring regional surface-mass anomalies from  
727 Gravity Recovery and Climate Experiment (GRACE) measurements of time-variable gravity,  
728 J. Geophys. Res., 107(B9), 2193. doi: 10.1029/2001JB000576.

729 Swenson, S., Wahr, J., 2006. Post-processing removal of correlated errors in GRACE data.  
730 Geophys. Res. Lett., 31: L23402. doi: 10.1029/2005GL025285.

731 Syed, T.H., Famiglietti, J.S., Rodell, M., Chen, J., Wilson, C.R., 2008. Analysis of terrestrial  
732 water storage changes from GRACE and GLDAS. Water Resour. Res. 44, W02433. doi:  
733 10.1029/2006WR005779.

734 Tang, Q., Zhang, X., Tang, Y., 2013. Anthropogenic impacts on mass change in North China.  
735 Geophys. Res. Lett. 40, 3924–3928. doi: 10.1002/grl.50790.

736 Tapley, B.D., Bettadpur, S., Watkins, M., Reigber, C., 2004a. The gravity recovery and  
737 climate experiment: Mission overview and early results. Geophys. Res. Lett. 31, L09607. doi:  
738 10.1029/2004GL019920.

739 van Dam, T., 2010. NCEP Derived 6 hourly, global surface displacements at  $2.5 \times 2.5$  degree  
740 spacing. <http://geophy.uni.lu/ncep-loading.html>.

741 van Dam, T., Blewitt, G., Heflin, M., 1994. Detection of atmospheric pressure loading using  
742 the Global Positioning System. J. Geophys. Res. 99(B12): 23939–23950.

743 van Dam, T., Collilieux, X., Wuite, J., Altamimi, Z., Ray, J., 2012. Nontidal ocean loading:  
744 Amplitudes and potential effects in GPS height time series. J. Geod. 86, 1043–1057. doi:  
745 10.1007/s00190-012-0564-5.

746 van Dam, T., Wahr, J., Lavallée, D., 2007. A comparison of annual vertical crustal  
747 displacements from GPS and Gravity Recovery and Climate Experiment (GRACE) over



748 Europe. J. Geophys. Res. 112, B03404. doi: 10.1029/2006JB004335.

749 Wahr, J., Khan, S.A., van Dam, T., Liu, L., van Angelen, J.H., van den Broeke, M.R.,

750 Meertens, C.M., 2013. The use of GPS horizontals for loading studies, with applications to

751 northern California and southeast Greenland. J. Geophys. Res. Solid Earth 118, 1795–1806.

752 doi: 10.1002/jgrb.50104.

753 Wahr, J., Molenaar, M., Bryan, F., 1998. Time-variability of the earth's gravity field:

754 Hydrological and oceanic effects and their possible detection using GRACE. J. Geophys. Res.

755 103, 30205–30230.

756 Wahr, J., Smeed, D.A., Leuliette, E., Swenson, S., 2014. Seasonal variability of the Red Sea,

757 from satellite gravity, radar altimetry, and in situ observations. J. Geophys. Res. Oceans 119,

758 5091–5104. doi: 10.1002/2014JC010161.

759 Wang, L.S., Chen, C., Du, J.S., Wang, Q.G., Sun, S.D., 2014. Impact of China large reservoir

760 water impoundment on spatial variability of coastal relative sea level. Earth Sci. (in Chinese

761 with an English abstract) 39(11), 1607–1616. doi: 10.3799/dqkx.2014.154.

762 Wang, L.S., Chen, C., Zou, R., Du, J.S., 2014. Surface gravity and deformation effects of

763 water storage changes in China's Three Gorges Reservoir constrained by modeled results and

764 in situ measurements. J. Appl. Geophys. 108, 25–34. doi: 10.1016/j.jappgeo.2014.06.007.

765 Wang, L.S., Chen, C., Zou, R., Du, J.S., Chen, X.D., 2014. Using GPS and GRACE to detect

766 seasonal horizontal deformation caused by loading of terrestrial water: A case study in the

767 Himalayas. Chinese J. Geophy. (in Chinese with an English abstract) 57(6), 1792–1804. doi:

768 10.6038/cjg20140611.

769 Wang, M., Li Q., Wang, F., Zhang, R., Wang, Y.Z., Shi, H.B., Zhang, P.Z., Shen, Z.K., 2011.



770 Far-field coseismic displacements associated with the 2011 Tohoku-oki earthquake in Japan  
771 observed by Global Positioning System. Chinese Sci. Bull., 56, 2419–2424. doi:  
772 10.1007/s11434-011-4588-7.  
773 Wang, X., de Linage, C., Famiglietti, J., Zender, C.S., 2011. Gravity Recovery and Climate  
774 Experiment (GRACE) detection of water storage changes in the Three Gorges Reservoir of  
775 China and comparison with in situ measurements. Water Resour. Res. 47, W12502. doi:  
776 10.1029/2011WR010534.  
777 Yi, L.X., Zhang, F., Xu, H., Chen, S.J., Wang W., Yu, Q., 2011. Land subsidence in Tianjin,  
778 China. Environ. Earth Sci. 62, 1151–1161. doi: 10.1007/s12665-010-0604-5.  
779 Zhao, B., Nie, Z.S., Huang, Y., Wang, W., Zhang, C.H., Tan, K., Du, R.L., 2014. Vertical  
780 motion of north China inferred from dense GPS measurements. J. Geodesy Geodyn. 34 (5),  
781 35–39 (in Chinese with an English abstract).  
782



783 **Table captions:**

784 **Table 1.** GPS Station information.

785

786 **Table 2.** Trends of TWS derived by GRACE and scaled GRACE during 2003–2009 and

787 2003–2012.

788



789 **Figure captions:**

790 **Figure 1.** Study region of North Plain China (NCP) showing locations of continuous GPS  
791 stations. White dots represent continuous GPS sites in the Crustal Movement Observation  
792 Network of China (CMONOC) and red stars represent the International GNSS Service (IGS)  
793 sites). Cities and provinces are labeled as follows: Beijing (BJ), Tianjin (TJ), Hebei province  
794 (HE), and Shanxi province (SX).

795

796 **Figure 2.** The 2003–2012 secular trend maps (cm/yr) of the terrestrial water storage (TWS)  
797 changes in North Plain China (NCP) and surrounding regions derived from GRACE data.  
798 Results have been destriped and smoothed with a 250-km Gaussian smoothing function.

799

800 **Figure 3.** Daily values of the vertical (positive upward) components of position, as measured  
801 at IGS GPS sites BJFS, ZHNZ, BJSN, JIXN and TAIN. The example of displacement due to  
802 atmospheric and non-tidal ocean loading at BJFS IGS sites are shown in (b).

803

804 **Figure 4.** Surface horizontal (north and east components) and vertical deformation modeled  
805 by GRACE in four IGS sites. (a) and (b) show the time series and trend rates of north and east  
806 components in BJFS, JIXN, TAIN and ZHNZ, respectively, (c) show the time series of  
807 vertical displacements.

808

809 **Figure 5.** Time series showing daily values (a) and fitting results (b) of the vertical (positive  
810 upward) components from GPS and GRACE-derived at five IGS GPS sites.



811

812 **Figure 6.** Comparison of annual amplitudes and initial phases between GPS (grey) and  
813 GRACE (red). The initial phases are counterclockwise from the east (reference time is  
814 2004.0).

815

816 **Figure 7.** Time series showing total terrestrial water storage (TWS) changes in the spatially  
817 averaged area (kernel) of the NCP estimated from CSR GRACE data. The dashed curve is the  
818 temporal smoothing result.

819

820 **Figure 8.** GRACE-derived smoothed (dash curves) and long-term (solid curves) vertical  
821 displacement time series due to load changes (a), the groundwater depletion contributions  
822 estimated from GRACE minus GLDAS data for smoothed (dash curves) and long-term (solid  
823 curves) vertical displacements (b), as measured at 25 GPS sites in NCP and its surrounding  
824 region. The grey background highlight part shows inflexion effects due to TWS changes in  
825 the vertical component.

826

827 **Figure 9.** Smoothed (dash curves) and long-term (solid curves) versions of daily values of the  
828 vertical (positive upward) component of position, as measured at 29 GPS sites in NCP and its  
829 surrounding region, (a) 5 IGS stations and (b) 24 CMONOC stations.

830

831 **Figure 10.** GPS (gray arrow, positive upward) and corrected GPS (red arrow, positive upward)  
832 vertical trend rate after subtracting the GRACE-derived long-term uplift rate due to load



833 changes and GIA effect between 2004 and 2009 (a), and between 2010 and 2013 (b).

834



835 **Table 1:**

836

Stations	Lat.	Lon.	Time	Annual Amplitude of vertical displacement (mm)		Annual Phase of vertical displacement (days) Reference time is 2004.0		Trend Rates of vertical displacement (mm/yr) 2004~2009		Trend Rates of vertical displacement (mm/yr) 2010~2013	
				GPS	GRACE	GPS	GRACE	GPS	GRACE	GPS	GRACE
BJFS*	39.6	115.8		2.50 $\pm$ 0.26	1.35 $\pm$ 0.24	40.09 $\pm$ 6.39	359.63 $\pm$ 10.73	1.47 $\pm$ 0.14	0.58 $\pm$ 0.06	-0.37 $\pm$ 0.23	0.26 $\pm$ 0.13
BJSH*	40.2	116.2		3.25 $\pm$ 0.23	1.25 $\pm$ 0.23	52.75 $\pm$ 4.20	1.00 $\pm$ 11.09	0.12 $\pm$ 0.12	0.53 $\pm$ 0.06	-0.94 $\pm$ 0.25	0.14 $\pm$ 0.13
JIXN*	40	117.5	2003	2.46 $\pm$ 0.22	1.32 $\pm$ 0.23	32.20 $\pm$ 5.11	359.72 $\pm$ 10.56	1.21 $\pm$ 0.12	0.53 $\pm$ 0.06	-0.19 $\pm$ 0.20	0.09 $\pm$ 0.13
TAIN*	36.2	117.1	~2013	3.31 $\pm$ 0.32	2.07 $\pm$ 0.39	16.44 $\pm$ 5.66	349.43 $\pm$ 11.36	0.18 $\pm$ 0.15	0.80 $\pm$ 0.09	0.46 $\pm$ 0.31	0.04 $\pm$ 0.16
ZHNZ*	34.5	113.1		2.38 $\pm$ 0.36	2.24 $\pm$ 0.43	28.18 $\pm$ 8.94	354.76 $\pm$ 11.39	0.04 $\pm$ 0.15	0.65 $\pm$ 0.10	2.55 $\pm$ 0.32	-0.35 $\pm$ 0.17
BJGB <sup>#</sup>	40.6	117.1		3.61 $\pm$ 0.41	1.25 $\pm$ 0.23	32.07 $\pm$ 6.58	4.25 $\pm$ 11.11		0.49 $\pm$ 0.06	0.25 $\pm$ 0.34	0.02 $\pm$ 0.13
BJYQ <sup>#</sup>	40.3	115.9		3.55 $\pm$ 0.41	1.23 $\pm$ 0.23	25.82 $\pm$ 6.87	3.34 $\pm$ 11.26		0.52 $\pm$ 0.06	-0.41 $\pm$ 0.34	0.14 $\pm$ 0.13
HAHB <sup>#</sup>	35.6	114.5		3.44 $\pm$ 0.42	2.13 $\pm$ 0.42	24.12 $\pm$ 6.93	349.19 $\pm$ 11.79		0.77 $\pm$ 0.10	-0.55 $\pm$ 0.27	-0.28 $\pm$ 0.17
HAJY <sup>#</sup>	35.1	112.4		2.28 $\pm$ 0.51	2.05 $\pm$ 0.44	9.28 $\pm$ 13.00	355.65 $\pm$ 12.80		0.84 $\pm$ 0.10	-0.30 $\pm$ 0.33	-0.40 $\pm$ 0.17
HECC <sup>#</sup>	40.8	115.8		2.49 $\pm$ 0.39	1.17 $\pm$ 0.23	9.25 $\pm$ 9.05	11.15 $\pm$ 1.81		0.49 $\pm$ 0.06	1.32 $\pm$ 0.25	0.06 $\pm$ 0.13
HECD <sup>#</sup>	41	117.9		4.09 $\pm$ 0.36	1.27 $\pm$ 0.23	40.28 $\pm$ 5.21	7.63 $\pm$ 11.09		0.45 $\pm$ 0.06	-0.68 $\pm$ 0.25	-0.07 $\pm$ 0.13
HECX <sup>#</sup>	38.4	116.9		4.57 $\pm$ 0.51	1.62 $\pm$ 0.29	41.20 $\pm$ 6.82	348.56 $\pm$ 10.80		0.73 $\pm$ 0.07	-20.85 $\pm$ 0.38	0.26 $\pm$ 0.14
HELQ <sup>#</sup>	38.2	114.3		2.06 $\pm$ 0.37	1.67 $\pm$ 0.28	30.89 $\pm$ 10.63	354.34 $\pm$ 9.95		0.68 $\pm$ 0.07	1.76 $\pm$ 0.26	0.31 $\pm$ 0.14
HELY <sup>#</sup>	37.3	114.7		2.65 $\pm$ 0.37	1.88 $\pm$ 0.33	10.54 $\pm$ 8.44	350.61 $\pm$ 10.56		0.79 $\pm$ 0.08	0.30 $\pm$ 0.27	0.11 $\pm$ 0.15
HETS <sup>#</sup>	39.7	118.2		1.59 $\pm$ 0.42	1.39 $\pm$ 0.24	279.75 $\pm$ 15.31	355.30 $\pm$ 10.28		0.53 $\pm$ 0.06	3.70 $\pm$ 0.32	0.07 $\pm$ 0.13
HEY <sup>#</sup>	40.1	114.1		3.40 $\pm$ 0.39	1.20 $\pm$ 0.23	2.92 $\pm$ 6.44	7.32 $\pm$ 11.44		0.49 $\pm$ 0.06	0.76 $\pm$ 0.30	0.29 $\pm$ 0.13
HEZJ <sup>#</sup>	40.8	114.9	2010	1.95 $\pm$ 0.35	1.13 $\pm$ 0.23	364.91 $\pm$ 10.74	15.62 $\pm$ 12.11		0.47 $\pm$ 0.06	1.06 $\pm$ 0.25	0.11 $\pm$ 0.13
NMTK <sup>#</sup>	40.2	111.2	~2013	3.37 $\pm$ 0.47	1.02 $\pm$ 0.23	8.85 $\pm$ 7.09	25.83 $\pm$ 13.67		0.37 $\pm$ 0.06	1.20 $\pm$ 0.37	0.51 $\pm$ 0.13
NMZL <sup>#</sup>	42.2	115.9		1.72 $\pm$ 0.39	1.15 $\pm$ 0.23	37.43 $\pm$ 14.85	30.16 $\pm$ 12.06		0.41 $\pm$ 0.06	-0.49 $\pm$ 0.28	-0.10 $\pm$ 0.13
SDJX <sup>#</sup>	35.4	116.3		2.36 $\pm$ 0.40	2.22 $\pm$ 0.41	39.05 $\pm$ 9.97	350.76 $\pm$ 11.00		0.71 $\pm$ 0.10	0.78 $\pm$ 0.33	-0.07 $\pm$ 0.17
SDZB <sup>#</sup>	36.8	117.9		3.59 $\pm$ 0.44	1.90 $\pm$ 0.37	25.65 $\pm$ 6.87	347.50 $\pm$ 11.50		0.79 $\pm$ 0.09	-1.12 $\pm$ 0.30	0.12 $\pm$ 0.16
SXCZ <sup>#</sup>	36.2	113.1		3.99 $\pm$ 0.47	1.93 $\pm$ 0.39	35.27 $\pm$ 6.48	352.64 $\pm$ 12.24		0.87 $\pm$ 0.09	0.22 $\pm$ 0.30	-0.22 $\pm$ 0.16
SXGX <sup>#</sup>	36.2	111.9		1.17 $\pm$ 0.51	1.81 $\pm$ 0.39	311.44 $\pm$ 26.46	359.06 $\pm$ 12.86		0.92 $\pm$ 0.09	3.17 $\pm$ 0.38	-0.17 $\pm$ 0.16
SXLF <sup>#</sup>	36	111.3		3.65 $\pm$ 0.48	1.79 $\pm$ 0.40	18.16 $\pm$ 7.77	363.02 $\pm$ 13.33		0.95 $\pm$ 0.10	1.21 $\pm$ 0.31	-0.19 $\pm$ 0.17
SXLQ <sup>#</sup>	39.3	114		3.63 $\pm$ 0.47	1.38 $\pm$ 0.24	25.49 $\pm$ 7.95	362.70 $\pm$ 10.45		0.54 $\pm$ 0.06	1.42 $\pm$ 0.33	0.39 $\pm$ 0.13
SXXX <sup>#</sup>	35.1	111.2		2.93 $\pm$ 0.54	1.98 $\pm$ 0.43	15.09 $\pm$ 10.44	363.17 $\pm$ 13.18		0.90 $\pm$ 0.10	1.30 $\pm$ 0.41	-0.36 $\pm$ 0.17
TJBD <sup>#</sup>	39.6	117.3		3.36 $\pm$ 0.48	1.38 $\pm$ 0.24	25.80 $\pm$ 7.38	355.65 $\pm$ 10.54		0.58 $\pm$ 0.06	-1.10 $\pm$ 0.33	0.16 $\pm$ 0.13
TJBH <sup>#</sup>	39	117.6		6.25 $\pm$ 0.45	1.49 $\pm$ 0.26	42.18 $\pm$ 9.56	350.10 $\pm$ 10.60		0.64 $\pm$ 0.06	-16.84 $\pm$ 0.37	0.20 $\pm$ 0.13
TJWQ <sup>#</sup>	39.3	117.1		5.08 $\pm$ 0.49	1.43 $\pm$ 0.25	0.11 $\pm$ 2.23	353.28 $\pm$ 10.58		0.62 $\pm$ 0.06	-44.46 $\pm$ 0.45	0.21 $\pm$ 0.13

837 \*IGS sites: the observation time between 2003 and 2013.

838 <sup>#</sup>CMONOC sites: the observation time between 2010 and 2013.

839

840

841

842



843

844 **Table 2:**

845

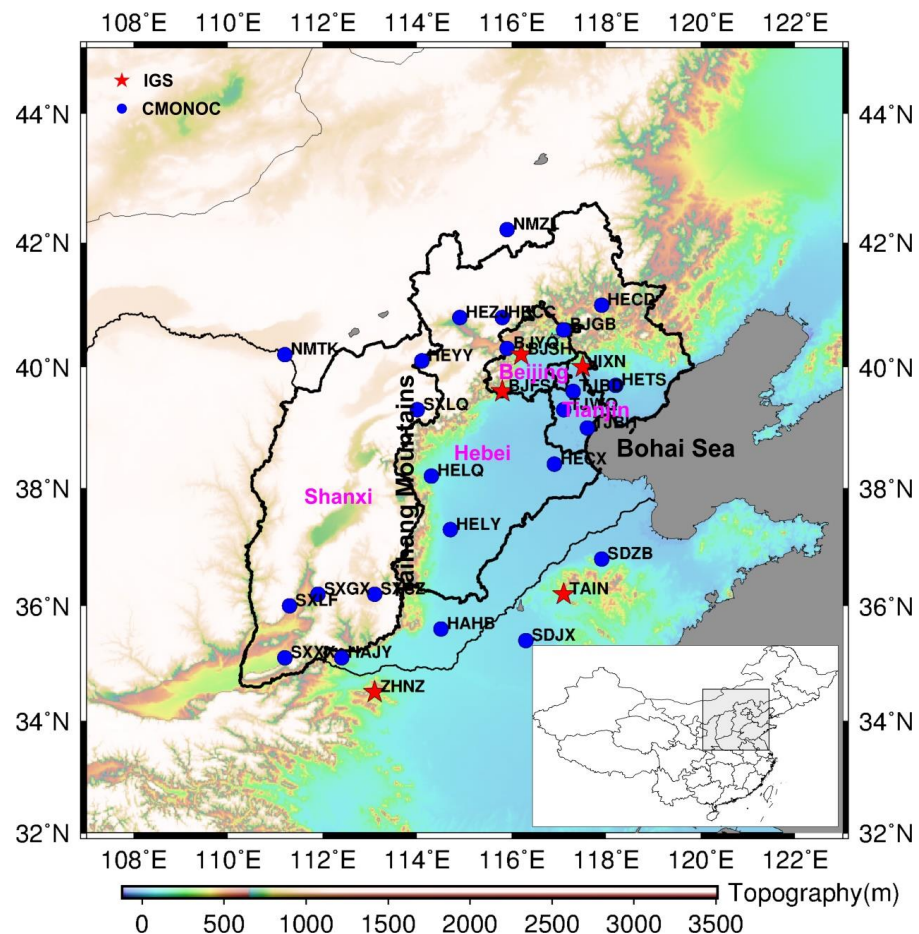
Time Span	GRACE Trend (cm/yr of the water thickness)	GRACE Scaled ( $\times 1/0.47$ ) Trend (cm/yr of the water thickness)	GRACE Scaled ( $\times 3.6626/0.47$ ) Trend (km $^3$ /yr of the mass)
2003~2009	$-1.62 \pm 0.39$	$-3.39 \pm 0.81$	$-12.42 \pm 3.15$
2003~2012	$-1.23 \pm 0.23$	$-2.57 \pm 0.49$	$-9.41 \pm 1.79$

846



847 **Figure 1:**

848

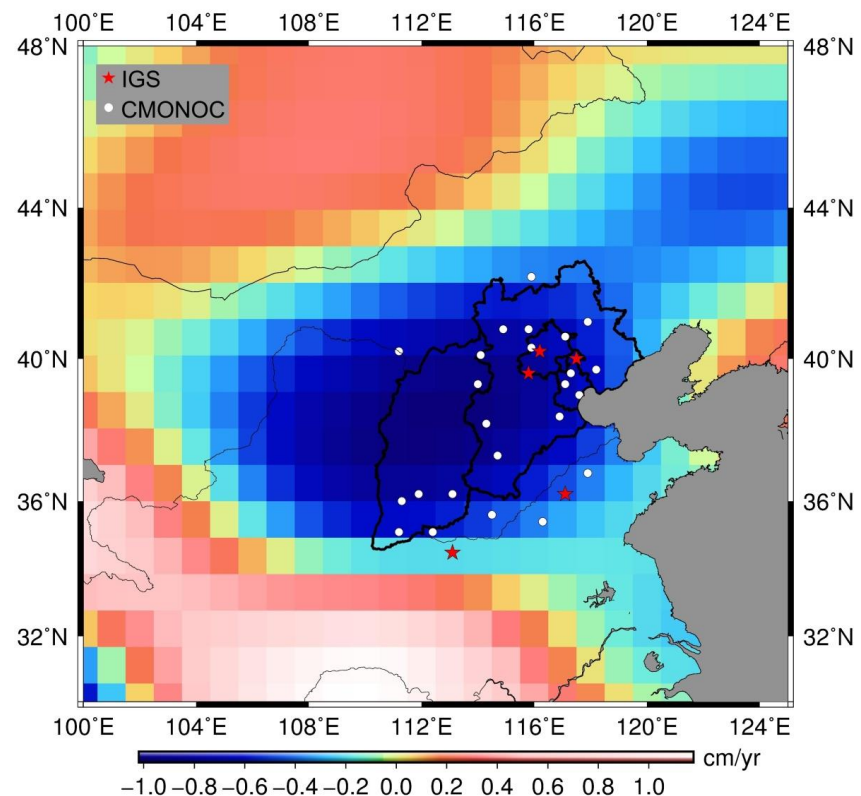


849



850 **Figure 2:**

851

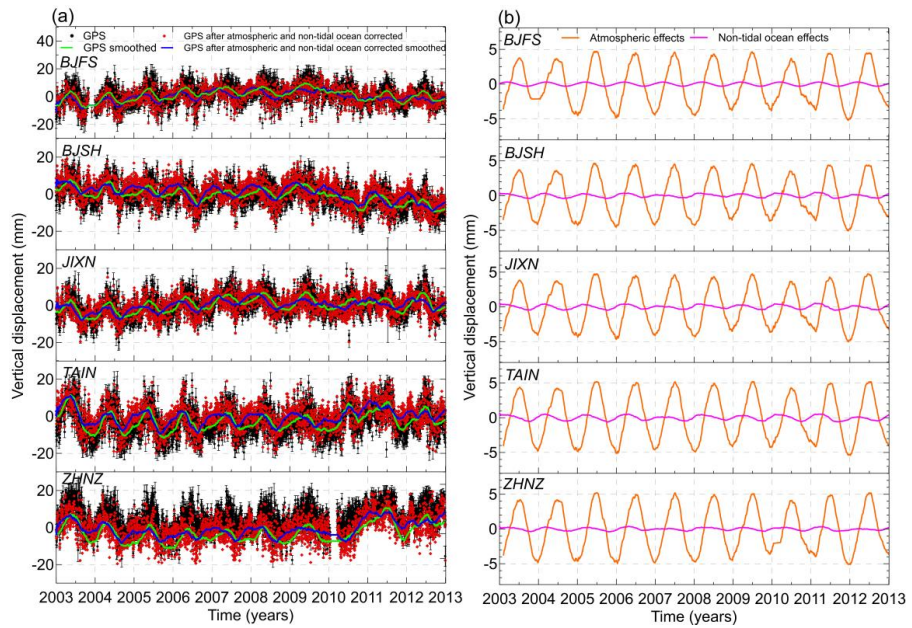


852



853 **Figure 3:**

854

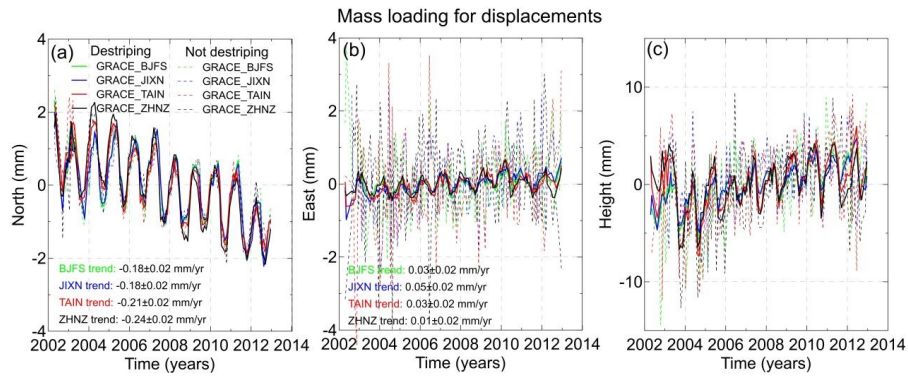


855



856 **Figure 4:**

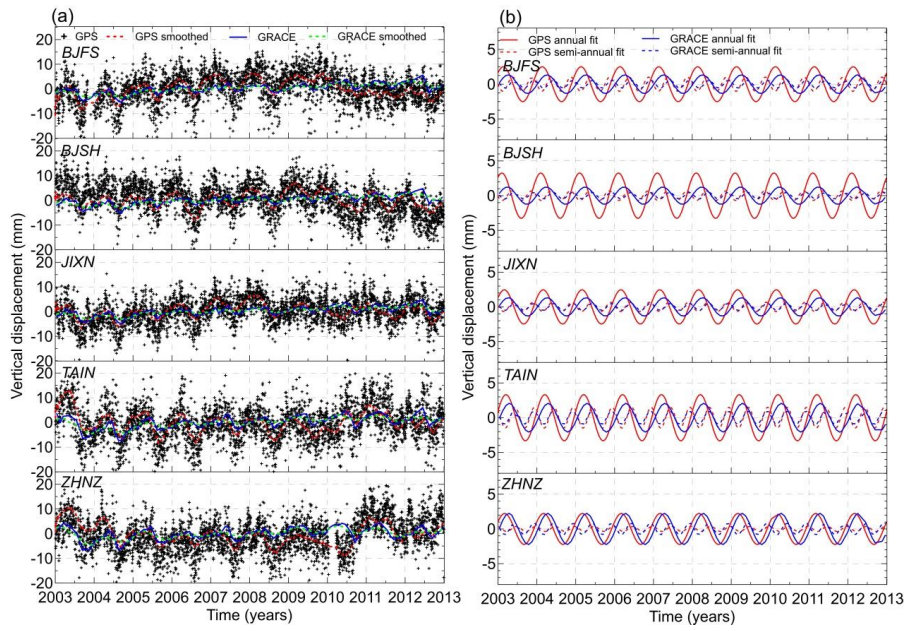
857



858



859 **Figure 5:**

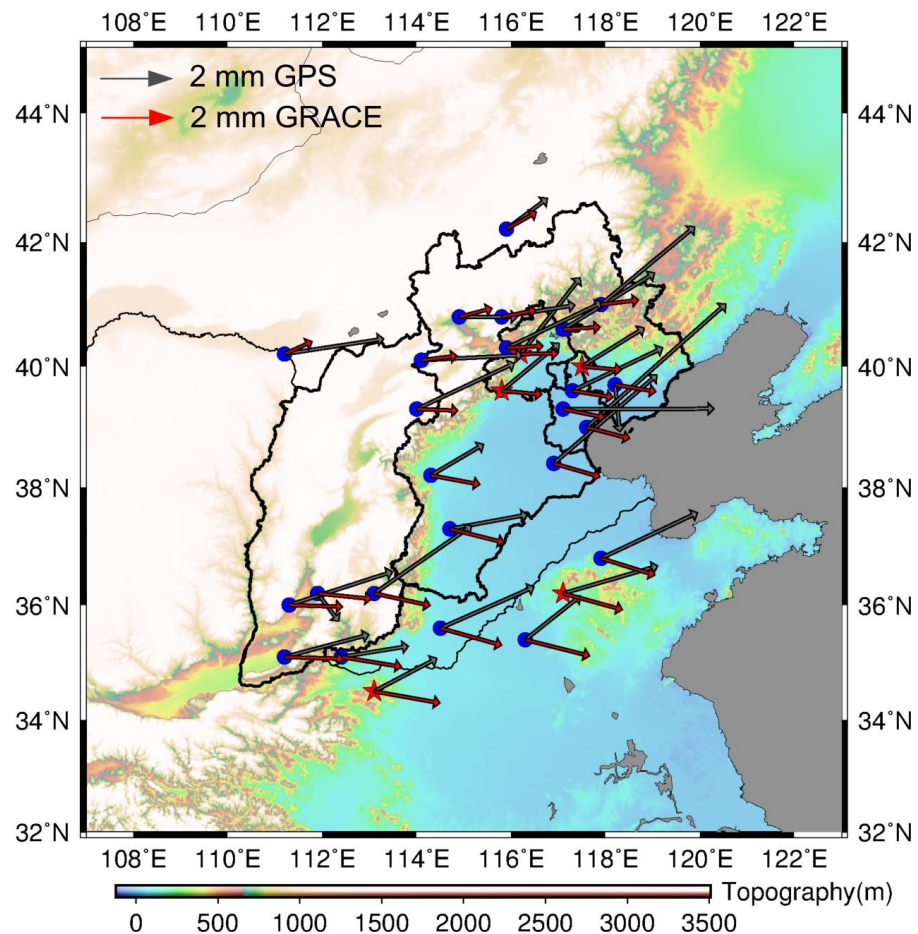


860



861 **Figure 6:**

862

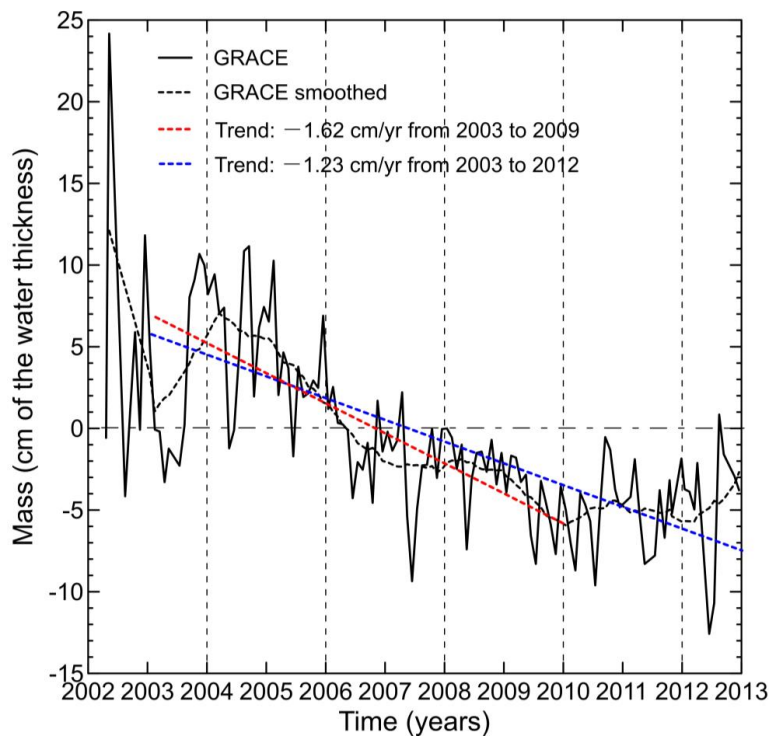


863



864 **Figure 7:**

865



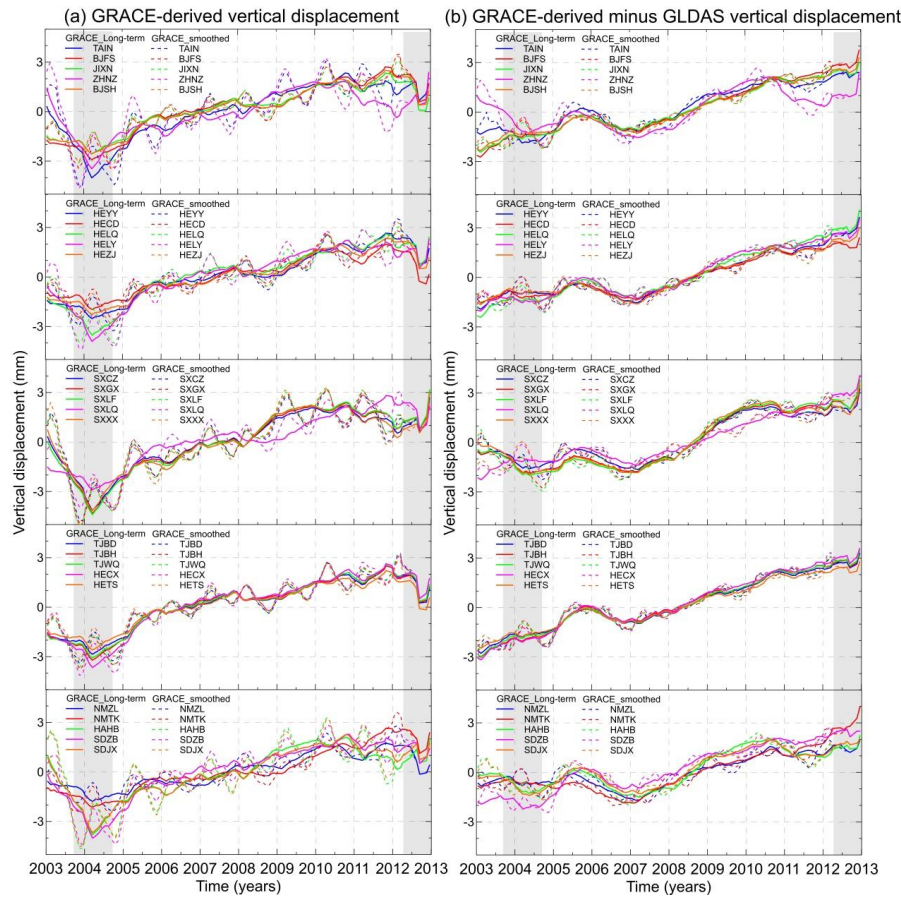
866

867



868 **Figure 8:**

869

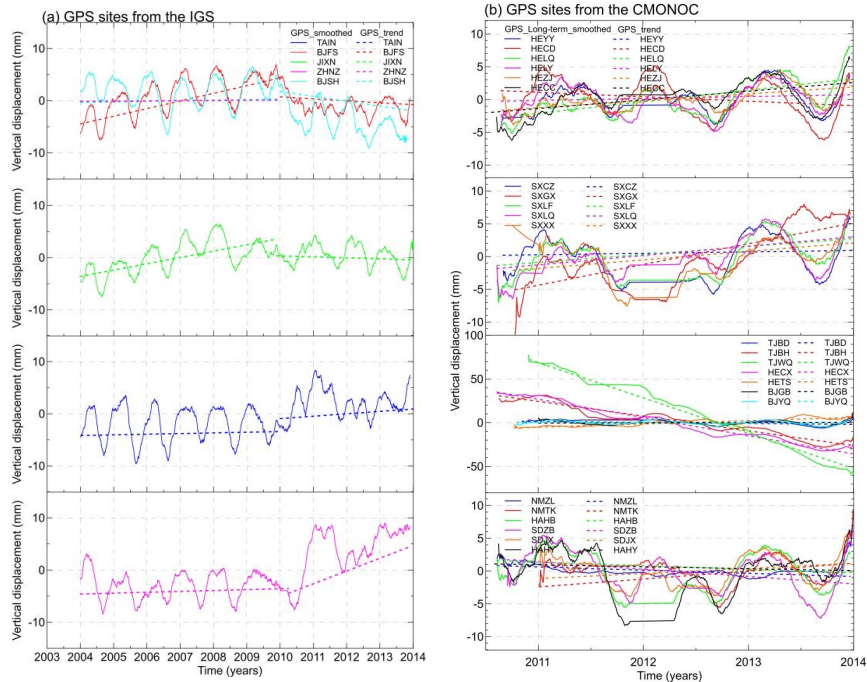


870



871 **Figure 9:**

872

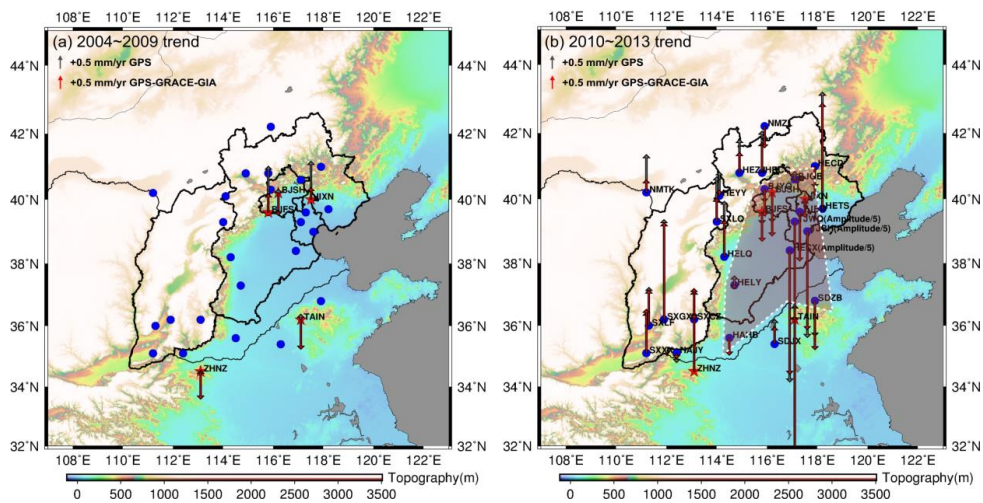


873



874 **Figure 10:**

875



876